RSC Sustainability

ROYAL SOCIETY OF CHEMISTRY

PAPER

View Article Online
View Journal | View Issue

Cite this: *RSC Sustainability*, 2025, **3**, 5641

Salinity resistance and wind-enhanced evaporation of biomass-derived foam for sustainable solar desalination

Wei Wang,[*ab] Xi Huan,[*abc] Jingnan Wang,[b] Siyuan Kang,[a] Yuheng Li,[ad] Ziyu Tian,[*c] Yining Li,[b] Xue Wang[b] and Jiang Fan[b]

Received 2nd September 2025
Accepted 5th November 2025

DOI: 10.1039/d5su00720h

rsc.li/rscsus

Solar-driven interfacial water evaporation is a promising sustainable desalination strategy, but most research has been predominantly focused on material innovation and evaporation rate enhancement, while little attention has been paid to the impact of convective airflow on salt resistance and energy efficiency. Herein, a novel biomass-derived porous evaporator based on carbonized wild rice root (CWRR) with interconnected microchannels was fabricated. The obtained CWRR-based evaporator exhibited remarkable salt tolerance, with a stable evaporation rate of 1.12 kg m^{-2} h^{-1} in 10 wt% NaCl solution over 6 h at efficiencies reaching 82.1%. The addition of convective airflow further enhanced the evaporation performance in 3.5 wt% NaCl at 2 m s^{-1} wind speed to yield a sustained evaporation rate of 2.19 kg m^{-2} h^{-1} over 6 h at efficiencies reaching 94.3%, highlighting remarkable energy utilization. Further analysis of the data revealed that moderate airflows could optimize vapor diffusion while improving salt deposition, and excessive wind velocities could disrupt the evaporation balance state, thereby accumulating salt and declining efficiency. Overall, solar desalination can be optimized by combining environmental airflow control with sustainable biomass materials as a promising novel strategy for future advanced desalination devices.

Sustainability spotlight

Freshwater scarcity demands sustainable solutions. This work upcycles waste wild rice root biomass into a carbon evaporator for solar desalination. This approach transforms agricultural waste into a valuable resource, promoting a circular economy. The material exhibits high solar absorption and efficient evaporation, providing an eco-friendly and low-cost path to clean water. This work directly aligns with SDG 6 (Clean Water and Sanitation), SDG 12 (Responsible Consumption and Production), and SDG 7 (Affordable and Clean Energy).

Introduction

The global crisis of freshwater supply has encouraged the development of sustainable desalination technologies. Solar-driven interfacial evaporation has emerged as a promising solution due to its renewable energy utilization and minimal carbon footprint.[1,2] Recent breakthroughs in photothermal materials, such as plasmonic nanoparticles, metal–organic frameworks (MOFs),[3–5] carbon-based materials,[6–8] and hydrogels,[9–11] have achieved remarkable solar-to-vapor efficiencies exceeding 80% under controlled laboratory conditions. These advancements have significantly improved freshwater production rates, making solar-driven desalination technology a viable alternative to energy-intensive conventional methods. However, the practical application of SIWE is still hindered by persistent salt accumulation on evaporative surfaces, particularly in hypersaline environments (>10 wt% salinity).[12–14] This can partially be solved by forming Janus structures and designing salt-backflows to mitigate salt crystallization but often compromises evaporation continuity or requires complex manufacturing.[15,16] Moreover, more attention has been paid to material innovations, while systemic challenges like dynamic environmental factors (air convective effect) are often overlooked. Additionally, while the influence of convective airflow on the evaporation equilibrium steady state and salt resistance performance of evaporators is not negligible, only a handful of studies have so far been reported.[17,18] Therefore, exploring evaporators with salt resistance and wind adaptability is vital for practical and advanced solar-driven evaporators.

[a]*School of Aeronautical Engineering, Shaanxi Polytechnic University, Xianyang, 712000, China. E-mail: wangwei05@sxpi.edu.cn; huanqian@sxpi.edu.cn*

[b]*Xianyang Key Laboratory of Solar Thermal Conversion Materials, Shaanxi Polytechnic University, Xianyang, 712000, China*

[c]*School of Opto-Electronical Engineering, Xi'an Technological University, Xi'an 710032, China. E-mail: 2193360756@qq.com*

[d]*College of Mechanical & Electrical Engineering, Shaanxi University of Science & Technology, Xi'an 710021, China*

Biomass-derived porous carbon materials have attracted increasing attention for practical uses owing to their natural abundance, inimitable pore structures, and exceptional light absorption.[19,20] Various studies have demonstrated that materials, such as carbonized wood, modified coconut fiber, and carbonized mushrooms could achieve evaporation rates of 1.2–1.5 kg m^{-2} h^{-1}, leveraging the inherent microchannels for passive salt rejection.[21,22] However, more focus has been paid to material synthesis, while little attention has been devoted to the influence of environmental factors on evaporation equilibrium states, including the convective airflow in improving the salt resistance of evaporators. Furthermore, the high cost and complex fabrication processes of chemically synthesized evaporators have limited their widespread adoption and mass production. By contrast, biomass materials sourced from nature are low-cost and readily available. For example, wild rice roots are often discarded as waste, making them available at low cost.[23–29] Additionally, wild rice roots are aquatic plants with exceptional natural water absorption capacity, making them promising materials for solar-driven evaporators.[30–33]

Herein, a novel salt-resistant evaporator based on carbonized wild rice root (CWRR) was engineered for self-desalting evaporation in a convective airflow environment. Two novelty aspects were explored. The first consisted of studying the pore structure of low-cost, naturally derived wild rice roots to supplement the pore design of biomass-derived evaporators, and the second dealt with exploring the impact of convective airflow on the evaporation equilibrium state of biomass evaporators. The optimized CWRR showed excellent light absorption (94.6%), resulting in average evaporation rates and photothermal conversion efficiencies of 1.27 kg m^{-2} h^{-1} and 85% in 3.5–10 wt% NaCl, respectively. The unique pore structure of CWRR enabled stable evaporation performance in 10 wt% NaCl for 6 hours. The influencing mechanism of gradient-intensity convective airflow (1, 2, and 4 m s^{-1}) on the salt tolerance of CWRR revealed CWRR achieving an average evaporation rate of 2.01 kg m^{-2} h^{-1} and 95% evaporation efficiency in 10 wt% NaCl under a 2 m s^{-1} wind speed, highlighting the ameliorating effect of convective airflow on reduction of thermal loss in the evaporator. The mechanisms of CWRR's evaporative equilibrium state under different convective airflow and salinities were also investigated, highlighting the significant effect of salinity/convective airflow on evaporation performance of environmentally adaptable desalination evaporators.

Experimental section

Material preparation

The wild rice root (WRR) material was purchased from a local supermarket in Xianyang City, Shaanxi Province, China. After procurement, the roots were cut into cuboid blocks (length 2 cm), followed by a pre-freezing process in a freeze dryer at −60 °C for 6 hours, and then freeze-dried for 24 hours to obtain a porous foam structure (Fig. S1 of the SI). The obtained porous foam maintained the overall structure of the initial WRR, with only the removal of the internal moisture while keeping the internal plant tissue intact. Subsequently, the freeze-dried samples were carbonized in a tubular furnace under controlled conditions of temperature rise to 600 °C at a heating rate of 5 °C min^{-1} for 2 hours to produce carbonized wild rice root (CWRR) (Fig. S1). CWRR still retained the internal pore structure recorded before carbonization, but the surface became black. Finally, the CWRR was thoroughly cleaned using ethanol and distilled water to remove any present impurities and residual contaminants.

Material characterization

The morphologies of the as-prepared CWRR samples were examined by scanning electron microscopy (ZEISS Sigma 300, Germany). The chemical elemental distribution and bonding states were characterized by X-ray photoelectron spectroscopy (XPS, Thermo Scientific ESCALAB 250Xi, USA). The chemical functional groups were identified by Fourier-transform infrared spectroscopy (FTIR, Thermo Fisher Scientific Nicolet iS20, USA). The optical properties were evaluated by UV-vis spectrometry UV-Vis-NIR spectrophotometry (Shimadzu UV-3600i Plus, USA) in the reflectance mode and the spectral range of 250–2500 nm. The quantitative elemental analyses and ionic concentrations in both simulated seawater and collected condensate were obtained by inductively coupled plasma optical emission spectrometry (ICP-OES, Agilent 5110). The porosity profiles of the CWRR were analyzed using a mercury porosimeter (AutoPore V 9500, USA). The CWRR's surface hydrophilicity was examined by a contact angle meter (Dataphysics OCA20, Germany).

Solar vapor evaporation measurements

The solar evaporation was carried out using an experimental setup (CEL-S500) solar simulator equipped with an AM 1.5 filter to replicate natural sunlight conditions. The solar irradiation intensity was quantified using a CEL-FZ-A power meter, and the mass variations of CWG during testing were tracked by a precision analytical balance (PTXFA300S, China). The thermographic measurements of the CWRR samples were acquired on a FLIR E4 thermal imaging system (FLIR Systems, USA). The wind effects on desalination performance were investigated by establishing controlled airflow environments with adjustable fans generating consistent wind velocities of 1, 2, and 4 m s^{-1}. The wind speed calibration and verification were performed using an AS-H10 anemometer (Aicevoos, China). All tests were executed under standardized laboratory conditions, with a temperature maintained at 25 °C and a relative humidity of 45%. Additionally, a self-built evaporation device was employed to carry and evaporate CWRR, using polystyrene foam as an insulation layer to prevent heat exchange between the CWRR and the underlying water. The detailed structure can be viewed in Fig. S2.

Results and discussion

Microstructure of CWRR

The capabilities of desalination evaporators, such as solar absorption efficiency, capillary-driven water transport, and anti-salt can be influenced by their microscopic pore

morphologies,[34] along with the diffusion of vapor and self-cleaning behavior of salt affected by the microchannel structures.[35] Hence, the top- and cross-sectional views of the as-prepared CWRR were characterized using SEM, and the results are shown in Fig. 1. Obviously, the CWRR maintained its overall structural integrity, with well-preserved natural pore morphology. The porous structure exhibited a highly developed cross-linked state, contributing to distinct morphological advantages (Fig. 1a and b), conducive to better solar evaporation performance. The deeply ravine-like channels would have dual functionality for achieving high solar absorption through multiple internal light reflections, as well as establishing continuous brine reflux pathways preventing localized salt saturation.[36] Furthermore, the vertically aligned internal microchannels would facilitate capillary-driven convective flows between upper evaporation zones and lower brine reservoirs (Fig. 1c and d).

Further surface structural characterization is displayed in Fig. S3 of the SI. Densely arrayed micrometric protrusions decorating side surfaces were formed, and micrometric protrusions expanded the transverse vapor diffusion channels in the evaporator, preventing internal clogging of vapor. Simultaneously, the formed protrusions increased the refraction path of sunlight on the side surfaces, enhancing the absorption of solar energy and significantly improving light-to-heat capability.[37] Such microscopic pores might enhance freshwater production rates and maintain salt concentration in evaporation regions.[6,18,38]

The pore distributions in CWRR showed a porosity of 90.18%, with pore diameters predominantly distributed between 100–200 μm and an average size of 11 μm (Fig. S4). The highly porous structure suggested the excellent steam diffusion capability, water transport capacity, and potentially favorable salt resistance of CWRR.[6]

Characterization and wettability of CWRR

The chemical composition and surface functionality of CWRR were identified by FTIR and XPS analyses. The FTIR spectra in Fig. 2a revealed distinct vibrational features corresponding to oxygen- and nitrogen-containing functional groups, including C–O at 1008.08 cm^{-1}, C═O at 1620.41 cm^{-1}, and O–H/N–H band at 3423.98 cm^{-1}.[39] Thus, CWRR contained hydrophilic functional groups. In Fig. 2b, the elemental composition of CWRR analyzed by XPS revealed the presence of C, O, and N elements. The fitting analysis of the C 1s spectrum (Fig. 2c) confirmed the presence of three characteristic peaks at C–C (284.78 eV), C–O (285.78 eV), and C═O (289.59 eV).[40] Moreover, the fitting analysis of the N 1s and O 1s spectra demonstrated existing functional groups of C–N (400.56 eV), –N═ (398.56 eV), C–O (532.84 eV), and C═O (531.67 eV) in CWRR (Fig. S5 and 6),[18] conducive to induced hydrophilic properties. The water contact angle testing of CWRR demonstrated rapid droplet absorption within 10 s, with a measured angle of 31.78°, confirming its advantageous hydrophilic properties (Fig. S7). The EDS analysis revealed surface elemental composition of CWRR consisting predominantly of C (82.95%), N (2.51%), and O (14.54%), indicating effective carbonization of the material (Fig. S8).

The wettability of CWRR was further explored by an infrared camera to monitor its wetting process in real-time. As depicted in Fig. 2d, the material reached thermal equilibrium with bulk

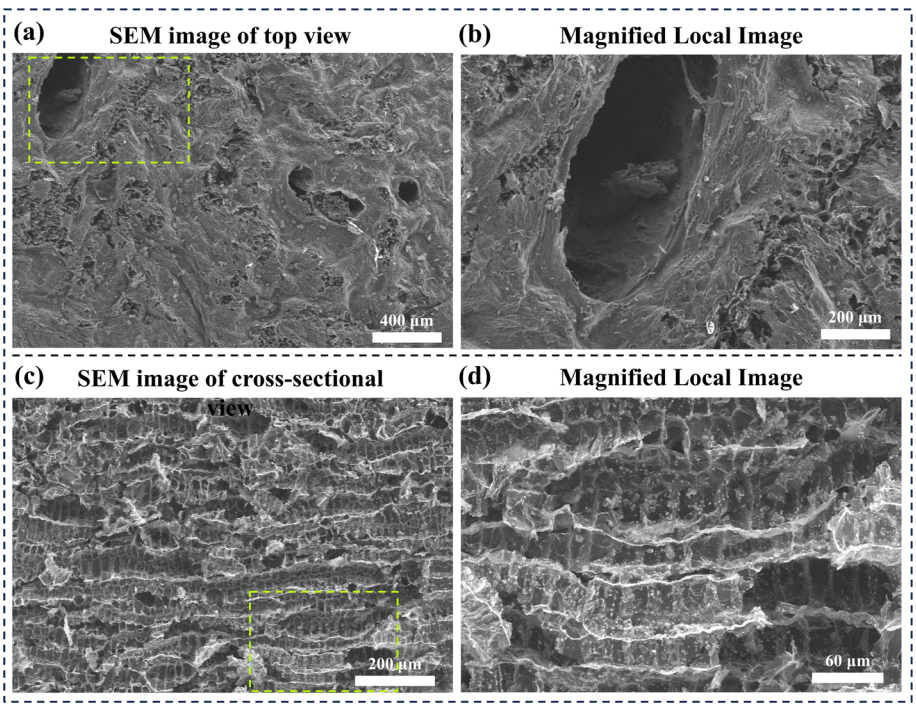

Fig. 1 SEM images of CWRR's (a and b) top, and (c and d) cross-sectional views. (b and d) Corresponding magnified images of the yellow rectangular regions.

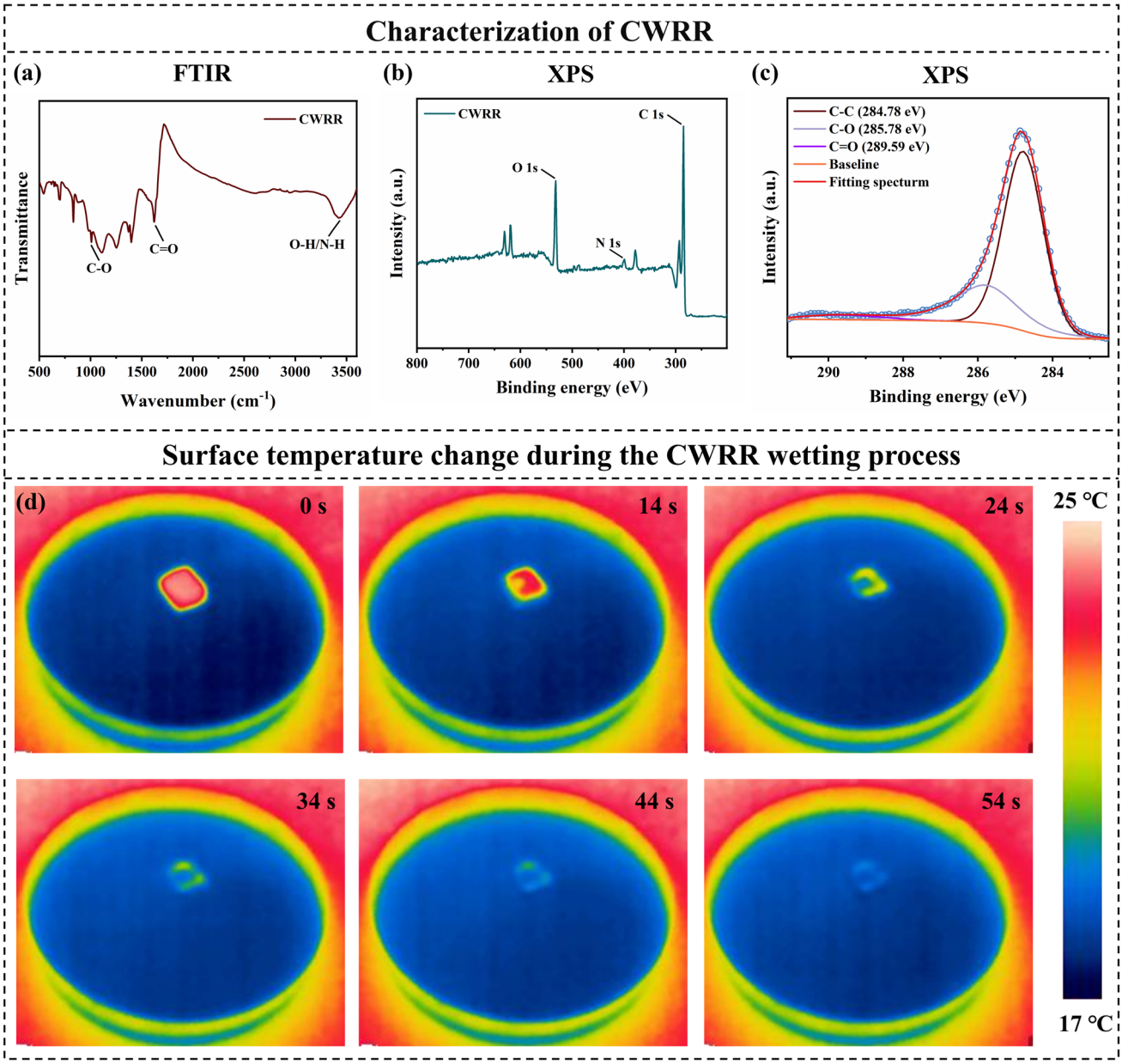

Fig. 2 Characterization and wettability analysis of CWRR. (a) FTIR and (b) XPS spectra of CWRR. (c) XPS peak fitting analysis of the C 1s region. (d) Infrared images of the surface temperature change during the CWRR wetting process.

water within approximately 54 s. Notably, the surface temperature of CWRR dropped rapidly at 10 s to approach the bulk water temperature (Fig. S9). Such rapid thermal equilibration can be attributed to the cross-linked porous structure, which enhanced water circulation and enabled efficient heat exchange between CWRR and the surrounding water. The efficient heat exchange capability arose from the interpenetrating channel structure and the hydrophilic functional groups. These properties may endow CWRR with rapid absorption and recycling of bulk water, implying a good anti-salt ability.

Salt resistance evaporation of CWRR

The power of solar-driven desalination would depend on photothermal conversion ability and sustained salt rejection capability. While vapor generation could achieve high solar absorption, salt crystallization at the evaporation interface may be challenging to eliminate, compromising long-term stability. Hence, continuous desalination tests were conducted under simulated brine conditions (3.5–20 wt% NaCl) to systematically evaluate CWRR's salt-resistant evaporation performance. As displayed in Fig. 3a, CWRR demonstrated excellent absorption of sunlight in the 200–2500 nm band (94.6% absorption), implying excellent light-to-heat capability. In Fig. 3b, the CWRR maintained a high steam generation rate across various salinity levels. The evaporation rates reached 1.35 kg m^{-2} h^{-1}, 1.18 kg m^{-2} h^{-1}, and 1.10 kg m^{-2} h^{-1} in 3.5, 10, and 20 wt% NaCl solutions, with corresponding photothermal conversion efficiencies of 86%, 85.6%, and 83.4% (Fig. 3c), respectively.

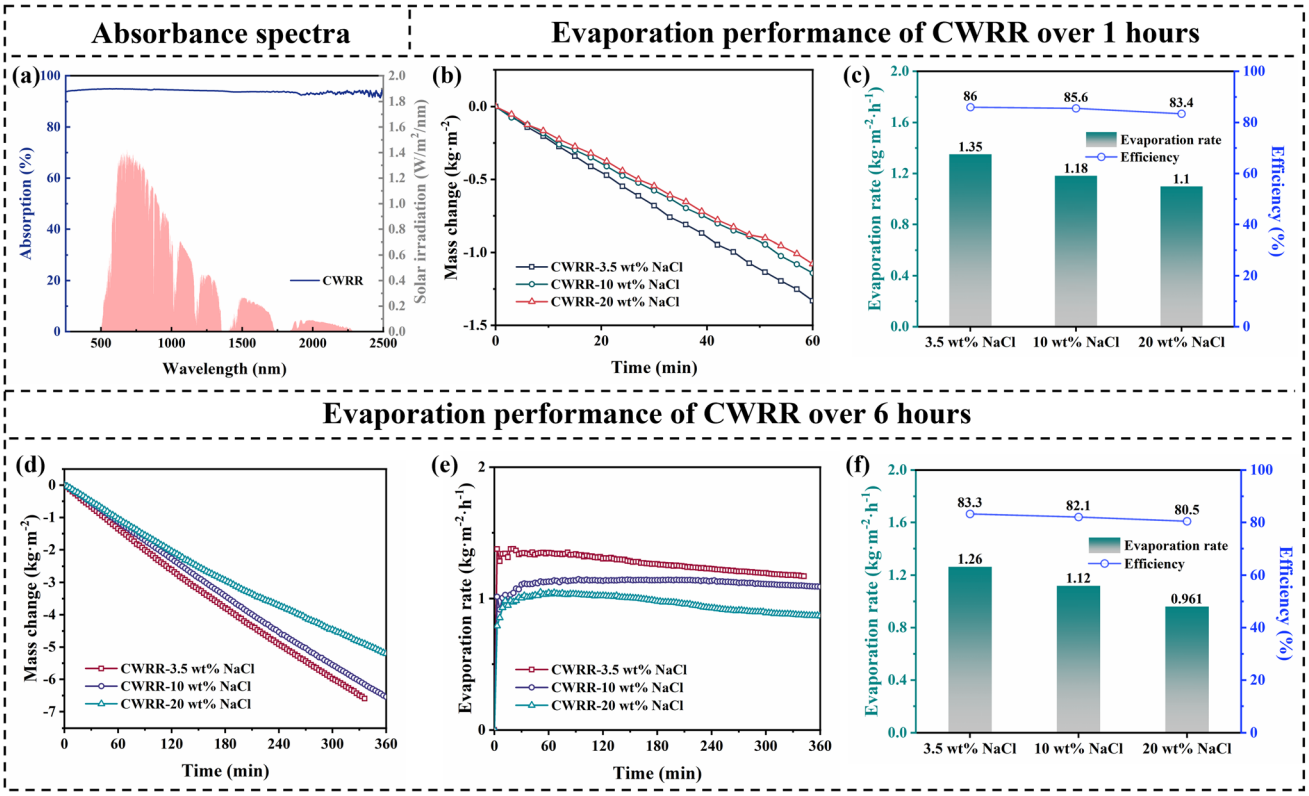

Fig. 3 Photothermal evaporation performance of CWRR. (a) Absorbance spectra of CWRR. (b) Mass changes, (c) evaporation rates and efficiencies of CWRR in 3.5, 10, and 20 wt% NaCl over 1 hour. (d) Mass changes, (e) evaporation rate curves, (f) evaporation rates and efficiencies of CWRR in 3.5, 10, and 20 wt% NaCl over 6 hours.

The salt resistance of CWRR was evaluated by monitoring its evaporation performance under continuous optical irradiation. As depicted in Fig. 3d, CWRR demonstrated stable evaporation characteristics during 6 hours of testing in both 3.5 and 10 wt% NaCl, maintaining steady evaporation rates (Fig. 3e) with final values of 1.26 kg m^{-2} h^{-1} (83.3% efficiency) and 1.12 kg m^{-2} h^{-1} (82.1% efficiency), respectively (Fig. 3f). However, a 12.7% decline in evaporation rate (from 1.10 to 0.961 kg m^{-2} h^{-1}) and a 2.9% reduction in efficiency (from 83.4% to 80.5%) were observed under extreme salinity conditions (20 wt% NaCl, Fig. 3f). Therefore, CWRR exhibited remarkable stability in ≤10 wt% NaCl environments but suffered significant performance degradation under hypersaline conditions (20 wt% NaCl), highlighting its operational limitations under extreme salinity scenarios.

The performance degradation under high salinity conditions may be attributed to disrupted evaporation equilibrium in the photothermal evaporator. This can be clarified by analyzing the temperature profiles and salt crystallization of CWRR. As illustrated in Fig. S10, CWRR exhibited relatively stable temperature variations across salinity gradients (3.5–20 wt% NaCl) during 1-hour evaporation tests. However, continuous evaporation revealed intensified temperature fluctuations in 20 wt% NaCl solution, with significant instability emerging at 240 min (Fig. S6), indicating severe disruption of the steady-state evaporation process. Such instability ultimately led to substantial salt accumulation on the evaporator surface after 6 hours (Fig. 4c). By contrast, CWRR maintained consistent temperature profiles (Fig. S11) and minimal surface salt crystallization (Fig. 4a and b) during continuous operation in respectively 3.5 and 10 wt% NaCl, demonstrating effective salt resistance up to 10 wt% NaCl. These findings confirmed the CWRR's sustained desalination capability in ≤10 wt% NaCl environments while revealing operational limitations under high salinity conditions (20 wt% NaCl), requiring supplementary strategies to enhance steam generation performance under extreme salinity scenarios.

Convective airflow for optimizing anti-salt performance

The occurrence of convective airflow would significantly influence natural seawater evaporation processes in terms of vapor diffusion, heat loss, and internal brine circulation, all affecting the evaporator balance state but often underestimated.[41,42] In particular, convective airflow of varying intensities may exert contrasting effects that can be beneficial or detrimental to salt circulation during evaporation. As a result, the CWRR's evaporation performances were systematically investigated under controlled wind speeds (1, 2, and 4 m s^{-1}) across NaCl concentrations ranging from 3.5–20 wt%, and the evaporation rates and efficiencies of CWRR under different wind speeds are summarized in Fig. 5a–c. At wind speed of 1 m s^{-1}, the system achieved evaporation rates of 1.53, 1.51, and 1.6 kg m^{-2} h^{-1} in 3.5, 10, and 20 wt% NaCl, respectively (Fig. 5a). Compared to the no-wind conditions, the additional convective flow effectively

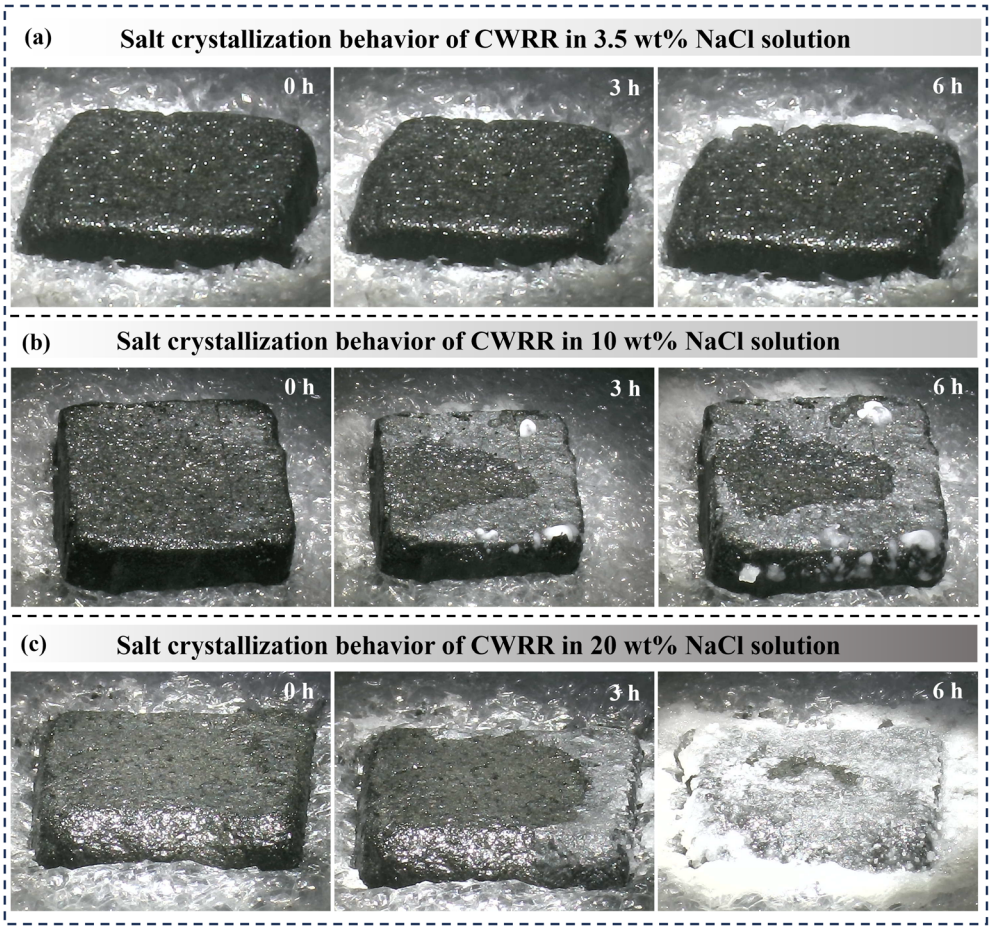

Fig. 4 Distribution of salt accumulation. Digital images of CWRR during 6 hours evaporation in (a) 3.5, (b) 10, and (c) 20 wt% NaCl. The CWRR samples in the figures all consisted of cubic blocks with a length and width of 2 cm × 2 cm.

enhanced the steam generation capacity of CWRR. Furthermore, substantial performance enhancement was observed at a wind speed of 2 m s^{-1}, with evaporation rates reaching 2.19, 1.96, and 2.05 kg m^{-2} h^{-1}, accompanied by efficiencies of 94.8%, 95%, and 92.3% (Fig. 5b), respectively. Compared to 1 m s^{-1}, the optimized convection improved the evaporation performance under 2 m s^{-1} conditions, with only a slightly decreased evaporation rate as a function of the increase in salinity, implying a better balance between steam escape and salt deposition. However, accelerated performance deterioration occurred as a function of salinity rise under wind speed of 4 m s^{-1}, declining from 2.63 kg m^{-2} h^{-1} (93.5% efficiency) at 3.5 wt% to 2.08 kg m^{-2} h^{-1} (88.3% efficiency) at 20 wt% NaCl (Fig. 5c).

Therefore, the increase in wind speed may enhance the evaporation ability, with a marked upward trend in evaporation rate noticed with the rise in wind velocity (Fig. 5d–f). However, the excessive wind-driven enhancement induced instability in the evaporative performance of the CWRR. Such fluctuation became particularly pronounced at wind speeds reaching 4 m s^{-1}, with the increase in surface salinity level as the main reason for the instability evaporation of CWRR. Collectively, these data demonstrated the direct influence of salinity on the equilibrium state of CWRR's evaporation process under excessive wind-accelerated conditions. Overall, 2 m s^{-1} airflow was determined as the optimal wind speed for the evaporation equilibrium of CWRR, which can counteract the salinity-induced evaporation performance inhibition (Fig. S12).[18,43] A careful analysis of the wind speed-dependent evaporation curves (Fig. 5d–f) demonstrated severe performance instability at a wind speed of 4 m s^{-1} under 20 wt% NaCl, indicating destructive airflow interference. By comparison, the moderate wind speed of 2 m s^{-1} resulted in an optimal relationship between evaporation and salt deposition, especially under harsh conditions of high salinity (Fig. 5f).

The above observations were further corroborated by CWRR's infrared thermal imaging, shown in Fig. 5g–i. Of note, the surface temperature (below 30 °C) of CWRR was lower under the influence of additional airflow on the evaporation interface than without wind speed (around 35 °C). In Fig. 5h, CWRR showed stable thermal curves at a wind speed of 2 m s^{-1}, contrasting the temperature fluctuations under a wind speed of 4 m s^{-1} (Fig. 5i, upward trend of surface temperature). Excess airflow disrupted the balance between evaporation and supply and aggravated the accumulation of salt ions at the evaporation interface. This resulted in rapidly deteriorating evaporation rates (Fig. 5f), and aggravated surface salt crystallization (Fig. S13) after only 3 hours of evaporation. Though minimal

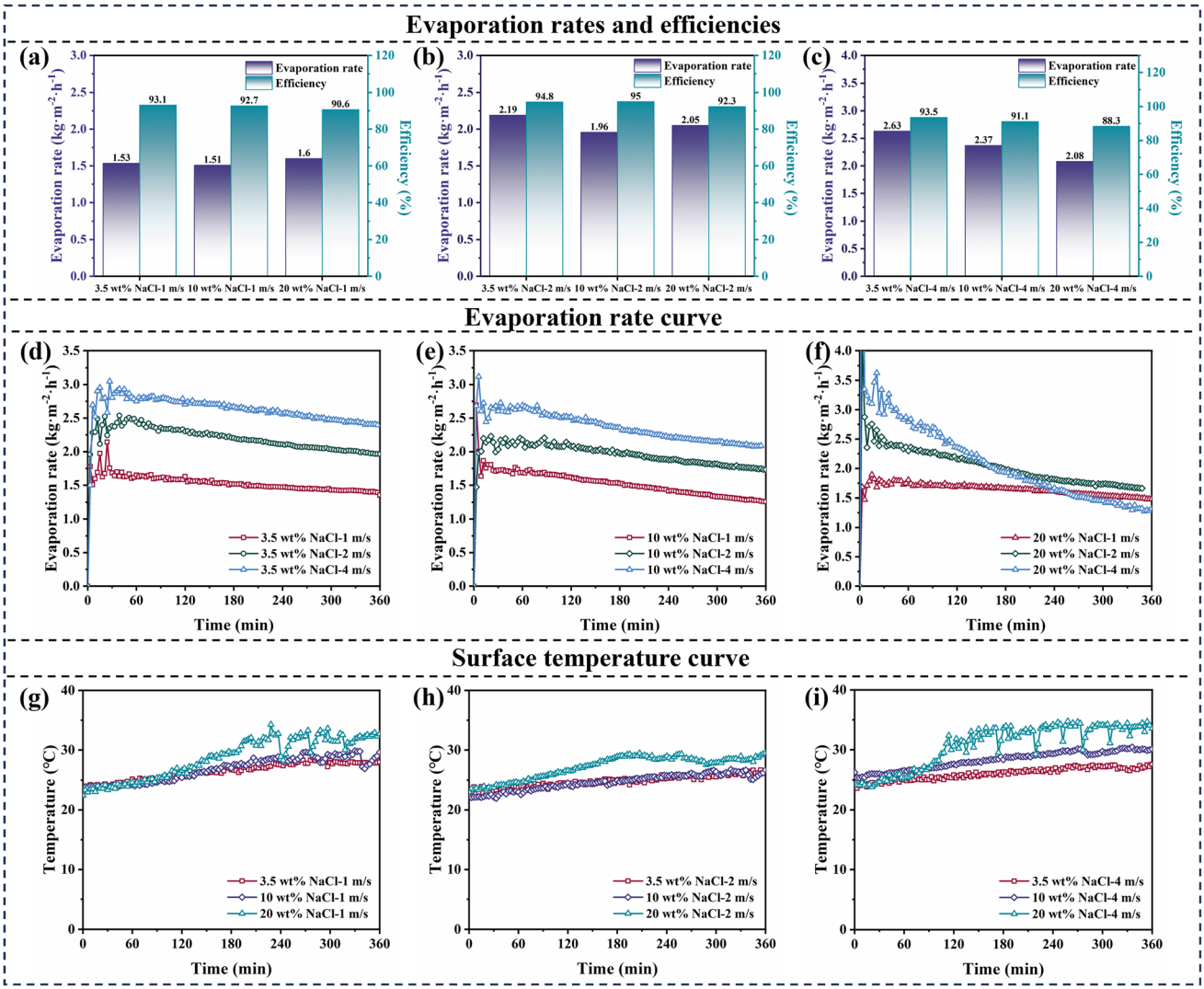

Fig. 5 Evaporation performances of CWRR under different convective airflows. Evaporation rates and efficiencies of CWRR in 3.5, 10, and 20 wt% NaCl at (a) 1, (b) 2, and (c) 4 m s^{-1} wind speeds over 6 hours. Evaporation rate curves of CWRR in 3.5, 10, and 20 wt% NaCl at (d) 1, (e) 2, and (f) 4 m s^{-1} wind speeds over 6 hours. Temperature change curves of CWRR in 3.5, 10, and 20 wt% NaCl at (g) 1, (h) 2, and (i) 4 m s^{-1} wind speeds over 6 hours.

surface salt deposition occurred at a wind speed of 1 m s^{-1} (Fig. 6), suboptimal internal water transport and vapor diffusion created non-equilibrium conditions, resulting in lower evaporation values (Fig. 5a). Overall, the most stable evaporative performance was maintained under 2 m s^{-1} airflow conditions, which can be attributed to the 2 m s^{-1} wind velocity promoting a dynamic equilibrium between steam generation and salt deposition/dissolution processes.[18]

The well-established photothermal mechanism of solar-driven interfacial seawater desalination would involve absorption of sunlight across a broad spectrum and its conversion into thermal energy.[44–48] Previous research on evaporators had primarily focused on minimizing heat losses (convective, conductive, and radiative). However, the unavoidable influence of convective air flow in practical outdoor applications[6,49,50] had reoriented recent research focus to exploring the effect of convective air on the regulation of the water-salt balance at the interfacial layer, building upon the conventional photothermal conversion mechanism.[18,51,52] Under continuous solar irradiation, water molecules present in the brine at the evaporator interface were continuously depleted. To maintain a stable state at the surface, the capillary channels of the evaporator continuously supplied brine to the interfacial layer (Fig. S14). Nevertheless, salt deposition was observed in the CWRR after 6 hours in a 20 wt% NaCl solution (Fig. 4c), which can be attributed to a mismatch between the rate of water evaporation and the rate of water supply from the capillary channels to the interfacial layer.[18,37,51,52] This gradually decreased the evaporation rate of CWRR in the 20 wt% NaCl solution over time.

Interestingly, the introduction of 1 m s^{-1} convective air effectively improved the evaporation performance of CWRR, with an evaporation rate increasing from 0.961 to 1.6 kg m^{-2} h^{-1} during 6 hours of continuous evaporation in 20 wt% NaCl solution (Fig. 3f and 5a). Despite the presence of partial salt

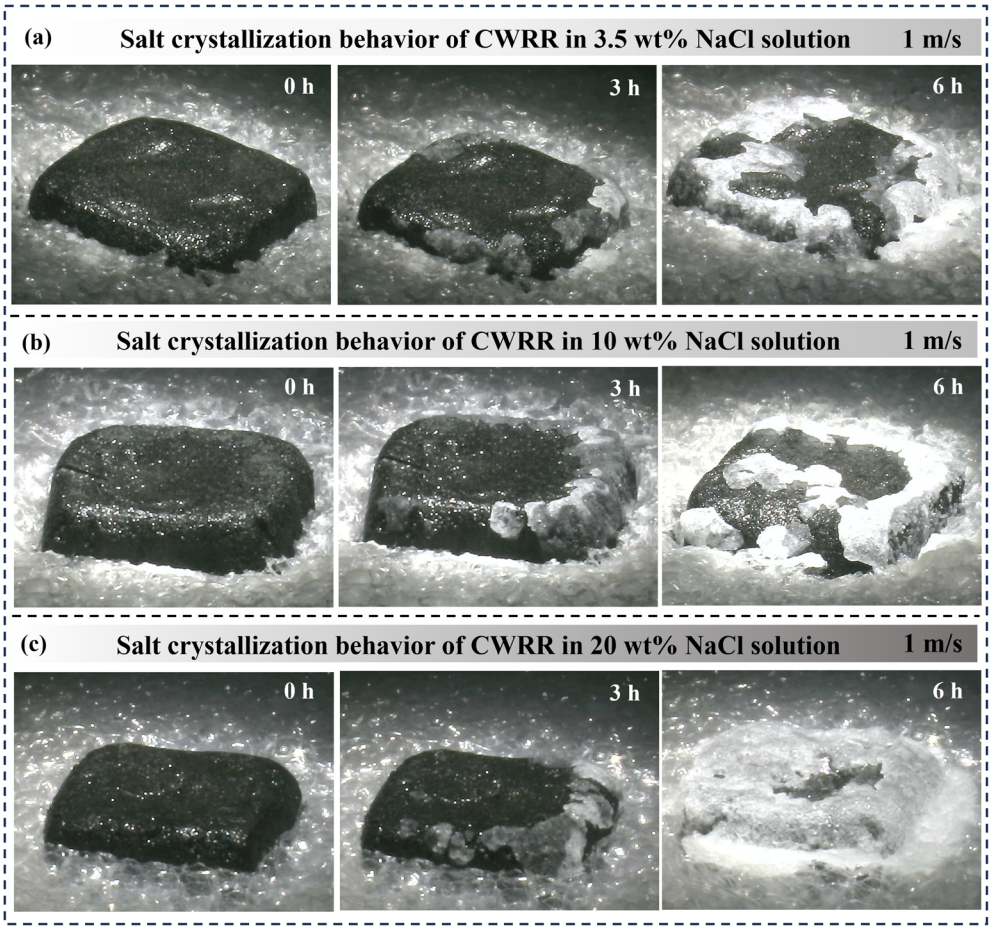

Fig. 6 Distribution of salt accumulation. Digital images of CWRR in (a) 3.5, (b) 10, and (c) 20 wt% NaCl at a wind speed of 1 m s^{-1}. The CWRR samples in the figures all consisted of cubic blocks with a length and width of 2 cm × 2 cm.

deposition on the CWRR surface, comparison of the evaporation rate curves and mass change curves of CWRR under windless conditions and 1 m s^{-1} wind speed showed an enhancement in its resistance to salt deposition (Fig. 3e and 5f). This can be explained by the wind speed reducing the pressure at the evaporator interface,[41,42,52] thereby enabling the internal capillary channels to supply water to the interface more rapidly (Fig. S14).[8,17,18] Nevertheless, the water supply capacity of the evaporator did not increase indefinitely as a function of wind speed, but obviously reached a threshold.[18,52] Consequently, the rise in wind speed to 4 m s^{-1} resulted in severe salt deposition of CWRR at the interface of 20 wt% NaCl solution than that under windless conditions (Fig. 4c and 6c).

Based on the above considerations, it can be concluded that wind speed greatly influenced the evaporation balance of the evaporator, with moderate convective airflow improving water evaporation. Under sustained evaporation in 20 wt% NaCl brine for 6 hours, the evaporation rate enhanced from 0.961 to 1.60 kg m^{-2} h^{-1}, with a solar-to-vapor efficiency reaching 90.6%. By contrast, excessive wind disturbance disrupted the liquid–vapor transition balance, potentially compromising the evaporation performance.

Outdoor desalination

Outdoor evaporation tests were conducted on December 24, 2024, in Xianyang City, Shaanxi Province (China, longitude 108.715° E, latitude 34.348° N) under natural solar irradiation (solar intensity 0.08–0.82 kW m^{-2}), as shown in Fig. 7a. The proposed CWRR demonstrated stable evaporation characteristic, achieving an average evaporation rate of 0.87 kg m^{-2} h^{-1} during 8 hours of continuous operation (Fig. 7b). Even at lower light intensities and temperatures, the CWRR maintained excellent freshwater yield performance (Fig. 7c). Meanwhile, CWRR maintained a self-cleaning surface after 8 hours of continuous evaporation in the natural environment (Fig. S15). Notably, visible vapor condensation was observed on the water-collection device surface, confirming effective phase-change management (Fig. 7d). Post-test ICP-OES analysis showed effectively removed ions from seawater in the presence of CWRR (Fig. 7e), reducing feedwater salinity from 9729 mg L^{-1} to 18.5 mg L^{-1}, in line with the World Health Organization permitted limit for clean water.[53] Therefore, the fabricated CWRR was capable of maintaining high evaporation flux under ambient conditions of 3 °C to 14.4 °C and RH of 23–56% to achieve practical desalination (Fig. S16).

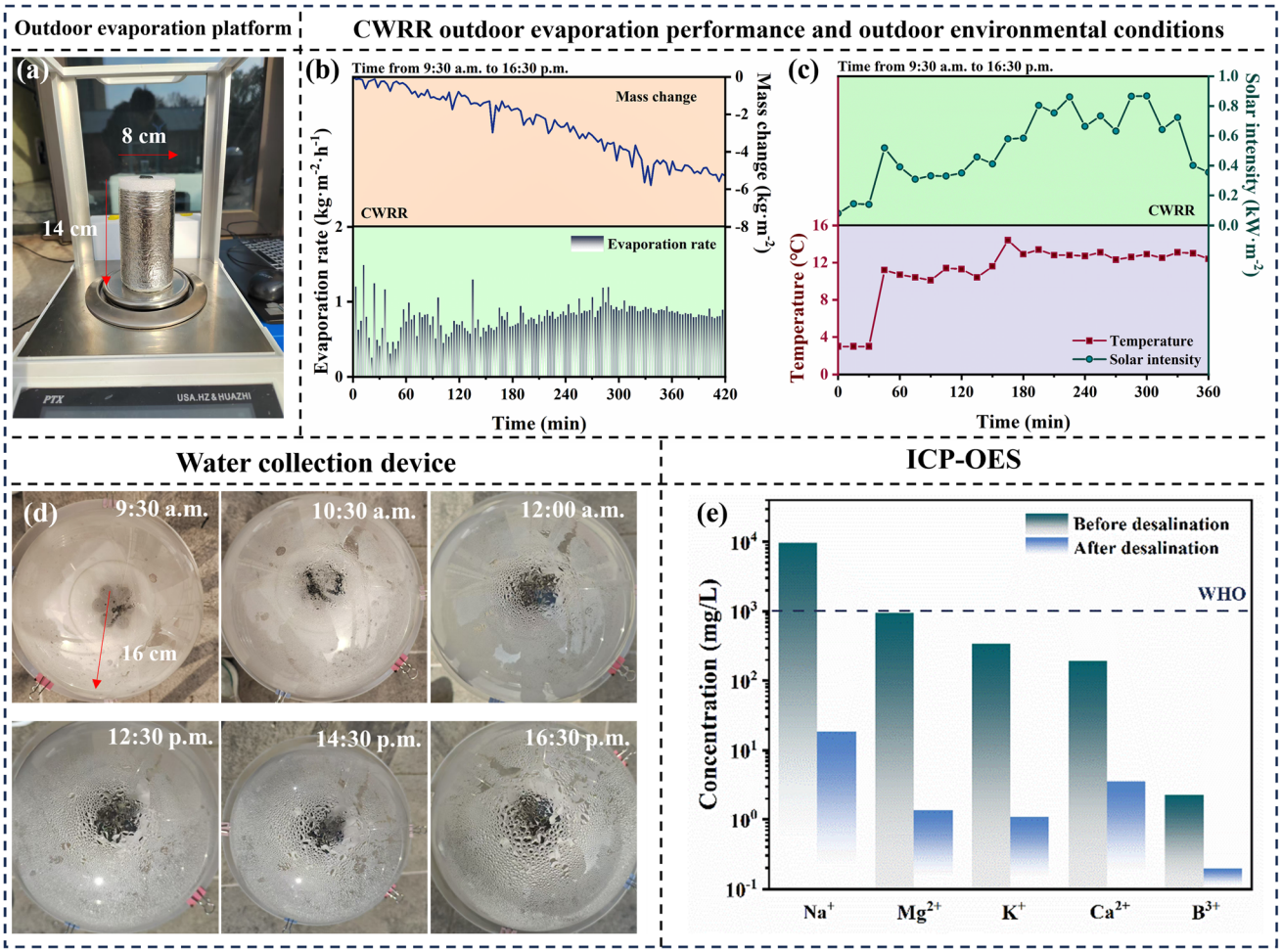

Fig. 7 Outdoor evaporation experiments. (a) Digital image of outdoor evaporation platform. (b) Outdoor mass change and evaporation rate curves of CWRR. (c) Outdoor temperature and solar intensity curves of CWRR. (d) Digital images of the water collection process in the outdoor evaporation device. (e) Ion concentrations before and after desalination of simulated seawater. In (d), 16 cm represents the inner radius of the spherical cover.

Conclusions

In summary, a novel porous carbonized wild rice root (CWRR) evaporator with excellent solar absorption (94.6%) and salt-rejection capability enabled by naturally interconnected pore architecture was successfully prepared and tested indoors and outdoors. The channel structure endowed CWRR with the best performances, achieving an evaporation rate of 1.35 kg m^{-2} h^{-1} with 86% efficiency in 3.5 wt% NaCl while maintaining self-cleaning functionality over 6 hours of continuous evaporation. The airflow optimization identified a moderate convective wind of 2 m s^{-1} as the optimal speed for enhancing the thermal management and vapor generation performance. Under this condition, CWRR achieved an evaporation rate of 2.19 kg m^{-2} h^{-1} (94.8% efficiency) in 3.5 wt% NaCl, with substantial improvements. Even in hypersaline environments, the evaporation rates and efficiencies increased from 0.96 kg m^{-2} h^{-1} (80.5%) to 2.05 kg m^{-2} h^{-1} (92.3%) in 20 wt% NaCl. Thus, controlling airflow positively modulated the CWRR's evaporation stability and salt resistance. However, airflow exceeding the evaporation system's critical threshold triggered counterproductive effects, enhancing salt crystallization due to disrupted interfacial equilibrium. Overall, novel insights into the dual role of convective airflow in solar desalination systems were provided, highlighting the necessity for controlled environmental regulation strategies for advanced desalination systems.

Conflicts of interest

The authors declare no conflicts of interest regarding the publication of this article.

Data availability

All data generated or analyzed during this study are included in this published article and its supplementary information (SI) files. Supplementary information is available. See DOI: https://doi.org/10.1039/d5su00720h.

Acknowledgements

This work was supported by the National Natural Science Foundation of China (52401098), the Natural Science Basic Research Program of Shaanxi (2025JC-YBQN-727), the Science and Technology Development Program of Weicheng District, Xianyang City (2024VCZY-005), and Science and Technology Innovation Team of Shaanxi Polytechnic University (KCTD2024-01).

References

1 F. S. Chien, C. Chi Hsu, I. Ozturk, A. Sharif and M. Sadiq, The role of renewable energy and urbanization towards greenhouse gas emission in top Asian countries: evidence from advance panel estimations, *Renewable Energy*, 2022, **186**, 207–216.

2 D. Wei, C. B. Wang, J. Zhang, H. Zhao, Y. Asakura, M. Eguchi, X. T. Xu and Y. Yamauchi, Water activation in solar-powered vapor generation, *Adv. Mater.*, 2023, **35**, 2212100.

3 U. Legrand, J. R. C. Sánchez, R. Boudreault, J. L. Meunier, P. L. G. Lauriault and J. R. Tavares, Fundamental thermodynamic properties of sorbents for atmospheric water capture, *Chem. Eng. J.*, 2022, **431**, 134058.

4 Y. Hu, Z. Fang, X. Y. Wan, X. Ma, Y. Q. Wang, M. Y. Dong, Z. Z. Ye and X. S. Peng, Ferrocene dicarboxylic acid ligand-exchanged hollow MIL-101(Cr) nanospheres for solar-driven atmospheric water harvesting, *ACS Sustainable Chem. Eng.*, 2022, **10**(19), 6446–6455.

5 W. L. Qi, C. H. Wang, J. Y. Yu, S. Adimi, T. J. Thomas, H. C. Guo, S. Q. Liu and M. H. Yang, MOF-Derived Porous Ternary Nickel Iron Nitride Nanocube as a Functional Catalyst toward Water Splitting Hydrogen Evolution for Solar to Chemical Energy Conversion, *ACS Appl. Energy Mater.*, 2022, **5**, 6155–6162.

6 W. Wang, Z. Y. Tian, X. Huan, Y. N. Li and P. Hu, Carbonized sweet potato-based evaporator for highly efficient solar vapor generation, *Energy Technol.*, 2024, **12**, 2300671.

7 J. H. Zhou, Y. F. Gu, P. F. Liu, P. F. Wang, L. Miao, J. Liu, A. Y. Wei, X. J. Mu, J. L. Li and J. Zhu, Development and evolution of the system structure for highly efficient solar steam generation from zero to three dimensions, *Adv. Funct. Mater.*, 2019, **29**, 1903255.

8 B. Shao, Y. D. Wang, X. Wu, Y. Lu, X. F. Yang, G. Y. Chen, G. Owensa and H. L. Xu, Stackable nickel-cobalt@polydopamine nanosheet based photothermal sponges for highly efficient solar steam generation, *J. Mater. Chem. A*, 2020, **8**, 11665–11673.

9 L. Li, N. He, B. Jiang, K. W. Yu, Q. Zhang, H. T. Zhang, D. W. Tang and Y. C. Song, Highly salt-resistant 3D hydrogel evaporator for continuous solar desalination via localized crystallization, *Adv. Funct. Mater.*, 2021, **31**, 2104380.

10 P. Liu, Y. B. Hu, X. Y. Li, L. Xu, C. Chen, B. Yuan and M. L. Fu, Enhanced solar evaporation using a scalable MoS_2-based hydrogel for highly efficient solar desalination, *Angew. Chem.*, 2022, **134**, 202208587.

11 T. X. Zhang, S. K. Jiao, J. X. Zhao, G. R. Gao, Y. Y. Yang and C. L. Guo, Solar water evaporation using porous cellulose polyacrylamide hydrogel with carbon-based material containing copper oxide prepared from after-use adsorbent, *Desalination*, 2022, **527**, 115576.

12 H. Zhang, X. K. Li, X. Y. Liu, Y. P. Du, W. Xie, S. Zheng, L. Yang, J. Shi and D. Jing, Biomimetic hydrogel with directional heat regulation for efficient solar desalination, *Chem. Eng. J.*, 2023, **473**, 145484.

13 J. Y. Li, X. Zhou, G. B. Chen, F. Wang, J. L. Mao, Y. Long, H. X. Sun, Z. Q. Zhu, W. D. Liang and A. Li, Evaporation efficiency monitoring device based on biomass photothermal material for salt-resistant solar-driven interfacial evaporation, *Sol. Energy Mater. Sol. Cells*, 2021, **222**, 110941.

14 H. Zhang, X. K. Li, S. Z. Zheng, J. Wen, J. Y. Zhou, R. Yang, W. M. Luo, L. Yang and X. H. Wu, The coral-inspired steam evaporator for efficient solar desalination via porous and thermal insulation bionic design, *SmartMat*, 2023, **4**, 1175.

15 Q. B. Xiao, Y. Zhu, Y. L. Xi, X. P. Kong, X. M. Ye, Z. Y. Zhang, C. P. Qiu, W. L. Xu, S. Cheng, J. Zhang, M. L. Jia, E. H. Sun, H. Z. Lin and J. Wang, Highly charged hydrogel with enhanced donnan exclusion toward ammonium for efficient solar-driven water remediation, *Chem. Eng. J.*, 2022, **430**, 133019.

16 J. Jiang, H. L. Jiang, Y. Xu, M. Chen and L. H. Ai, Janus Co@C/NCNT photothermal membrane with multiple optical absorption for highly efficient solar water evaporation and wastewater purification, *Colloids Surf., A*, 2022, **647**, 128960.

17 Y. D. Wang, X. Wu, T. Gao, Y. Lu, X. F. Yang, G. Y. Chen, G. Owens and H. L. Xu, Same materials, bigger output: A reversibly transformable 2D–3D photothermal evaporator for highly efficient solar steam generation, *Nano Energy*, 2021, **79**, 105477.

18 W. Wang, Z. Y. Tian, N. R. He, X. Huan, J. Fan and Y. N. Li, Biomass derived evaporator with highly interconnected structure for eliminating salt accumulation in high-salinity brine, *Desalination*, 2024, **574**, 117232.

19 P. Sun, W. Zhang, I. Zada, Y. X. Zhang, J. J. Gu, Q. L. Liu, H. L. Su, D. Pantelić, B. Jelenković and D. Zhang, 3D-structured carbonized sunflower heads for improved energy efficiency in solar steam generation, *ACS Appl. Mater. Interfaces*, 2020, **12**, 2171–2179.

20 Z. T. Li, C. Wang, T. Lei, H. Ma, J. Su, S. Ling and W. Wang, Arched Bamboo Charcoal as Interfacial Solar Steam Generation Integrative Device with Enhanced Water Purification Capacity, *Adv. Sustainable Syst.*, 2019, **3**, 1800144.

21 Q. Zhang, L. P. Ren, X. F. Xiao, Y. L. Chen, L. J. Xia, G. M. Zhao, H. J. Yang, X. B. Wang and W. L. Xu, Vertically aligned Juncus effusus fibril composites for omnidirectional solar evaporation, *Carbon*, 2020, **156**, 225–233.

22 N. Xu, X. Z. Hu, W. C. Xu, X. Q. Li, L. Zhou, S. N. Zhu and J. Zhu, Mushrooms as efficient solar steam-generation devices, *Adv. Mater.*, 2017, **29**, 1606762.

23 M. Zaed, J. Cherusseri, R. Saidur, K. H. Tan and A. K. Pandey, Synthesis and characterization of hierarchical Ti_3C_2Tx MXene/graphitic-carbon nitride/activated carbon@luffa sponge composite for enhanced water desalination, *Open Ceram*, 2024, **19**, 100645.

24 M. Zaed, K. H. Tan, R. Saidur, A. K. Pandey and J. Cherusseri, Low-cost synthesis of Ti3C2Tx MXene-based sponge for solar steam generation and clean water production, *Ceram. Int.*, 2024, **50**, 27910–27922.

25 S. A. Thomas, J. Cherusseri, D. N. Rajendran and R. Saidur, Graphitic carbon Nitride and their derivatives, in *Handbook of Functionalized Carbon Nanostructures: from Synthesis Methods to Applications*, ed. A. Barhoum and K. Deshmukh, Springer International Publishing, 2023, pp. 1–38.

26 S. A. Thomas, J. Cherusseri, D. N. Rajendran and R. Isaac, Functionalized carbon nanostructures for wastewater treatments. in *Handbook of Functionalized Carbon Nanostructures: from Synthesis Methods to Applications*, ed, A. Barhoum and K. Deshmukh, Springer International Publishing, 2023, pp. 1–44.

27 S. A. Thomas, J. Cherusseri and D. N. Rajendran, Loofah sponge: a sustainable material for wastewater desalination, *RSC Sustainability*, 2025, **3**, 2806–2832.

28 M. Zaed, R. Saidur, A. K. Pandey, M. Kadhom, K. H. Tan, J. Cherusseri and N. Abdullah, Utilization of recycled materials for low-cost MXene synthesis and fabrication of graphite/MXene composite for enhanced water desalination performance, *Sep. Purif. Technol.*, 2025, **354**, 129055.

29 M. Zaed, R. Saidur, A. M. Saleque, K. H. Tan, J. Cherusseri, A. K. Pandey and M. M. Kabir, Unlocking desalination's potential: Harnessing MXene composite for sustainable desalination, *Chem. Eng. J.*, 2024, **500**, 156910.

30 M. Zaed, J. Cherusseri, K. H. Tan, R. Saidur and A. K. Pandey, Hierarchical Ti_3C_2Tx MXene@Honeycomb nanocomposite with high energy efficiency for solar water desalination, *Chemosphere*, 2024, **366**, 143459.

31 M. Zaed, J. Cherusseri, R. Saidur, K. H. Tan, A. K. Pandey and N. Abdullah, Synthesis of Ti_3C_2Tx MXene@Carbon-Enhanced cellulose fiber composite-based photothermal absorber for sustainable water desalination, *Mater. Today Sustainability*, 2024, **28**, 100971.

32 K. Y. Yuan, Y. Shu, F. Y. Chu, C. B. He, Z. R. Xiang, X. T. Fu, H. Q. Wang and D. D. Ye, Microfluidic-mediated orientation nanoengineering for enhanced osmotic energy harvesting, *Nano Lett.*, 2025, **25**, 8939–8947.

33 L. Y. Zhang, Z. H. Yuan, X. T. Fu, S. Shi, X. Chen, P. Chen and D. D. Ye, Biomass-derived gradient and aligned structured aerogel for sustainable agricultural irrigation, *Nano Lett.*, 2025, **25**, 5383–5390.

34 H. Zhang, W. M. Luo, Y. P. Du, H. Shi, G. Y. Zeng, X. X. Yan and X. K. Li, The g-C_3N_4 decorated carbon aerogel with integrated solar steam generation and photocatalysis for effective desalination and water purification, *Desalination*, 2023, **564**, 116821.

35 L. Zhou, Y. L. Tan, J. Y. Wang, W. C. Xu, Y. Yuan, W. S. Cai, S. N. Zhu and J. Zhu, 3D self-assembly of aluminium nanoparticles for plasmon-enhanced solar desalination, *Nat. Photonics*, 2016, **10**, 393–398.

36 H. Zhang, Y. P. Du, D. W. Jing, L. Yang, J. Y. Ji and X. K. Li, Integrated Janus evaporator with an enhanced donnan effect and thermal localization for salt-tolerant solar desalination and thermal-to-electricity generation, *ACS Appl. Mater. Interfaces*, 2023, **15**, 49892–49901.

37 X. Huan, W. Wang, C. Wang, Z. Y. Tian and Y. H. Li, Plasmonic nanomaterials for versatile solar energy conversion applications, *ACS Omega*, 2025, **10**, 28615–28629.

38 H. Zhang, X. K. Li, S. Z. Zheng, J. Wen, J. Y. Zhou, R. Yang, W. M. Luo, L. Yang and X. H. Wu, The coral-inspired steam evaporator for efficient solar desalination via porous and thermal insulation bionic design, *SmartMat*, 2023, **4**, e1175.

39 Y. Sun, Z. B. Zhao, G. Y. Zhao, L. X. Wang, D. Z. Jia, Y. Z. Yang, X. G. Liu, X. Z. Wang and J. S. Qiu, High performance carbonized corncob-based 3D solar vapor steam generator enhanced by environmental energy, *Carbon*, 2021, **179**, 337–347.

40 H. T. Zhang, L. Li, B. Jiang, Q. Zhang, J. Ma, D. W. Tang and Y. C. Song, Highly thermally insulated and superhydrophilic corn straw for efficient solar vapor generation, *ACS Appl. Mater. Interfaces*, 2020, **12**, 16503–16511.

41 P. Wu, X. Wu, Y. D. Wang, H. L. Xu and G. Owens, Towards sustainable saline agriculture: Interfacial solar evaporation for simultaneous seawater desalination and saline soil remediation, *Water Res.*, 2022, **212**, 118099.

42 Y. Q. Chen, J. J. Hao, J. Xu, Z. S. Hu, H. F. Bao and H. L. Xu, Pickering emulsion templated 3D cylindrical open porous aerogel for highly efficient solar steam generation, *Small*, 2023, **19**, 2303908.

43 X. H. Liu, Z. C. Liu, D. D. Mishra, Z. H. Chen, J. Zhao and C. Q. Hu, Evaporation rate far beyond the input solar energy limit enabled by introducing convective flow, *Chem. Eng. J.*, 2022, **429**, 132335.

44 C. Ma, W. K. Wang, Q. Chen, R. R. Zhang, R. H. Yan, Z. Jia, X. L. Zhang, W. H. Zhang, L. Wang and C. B. Wang, Repurposing facial tissue waste to construct flexible hierarchical MOF-based photothermal material with lower evaporation enthalpy for high efficient solar-driven seawater desalination and wastewater purification, *Desalination*, 2025, **600**, 118472.

45 W. K. Wang, C. Ma, Z. Jia, Q. Chen, R. R. Zhang, X. L. Zhang, J. K. Zhu and C. B. Wang, Hierarchical TiO_2-coated metal-organic framework-derived carbon material for efficient co-generation of drinkable water and electricity, *Desalination*, 2025, **593**, 118256.

46 C. Ma, W. K. Wang, Q. Chen, Z. Jia, X. L. Zhang, J. Shi, J. K. Zhu, R. R. Zhang and C. B. Wang, Flexible hierarchical polypyrrole-coated Cu-BTC MOFs photothermal textile for efficiently solar water evaporation

and wastewater purification, *Chem. Eng. J.*, 2024, **480**, 148248.

47 C. Ma, W. K. Wang, Z. Jia, J. Zhang and C. B. Wang, Recent progress on emerging porous materials for solar-driven interfacial water evaporation, *Energy Technol.*, 2023, **11**, 2300263.

48 J. L. Wang, W. K. Wang, J. G. Li, X. Y. Mu, X. Y. Yan, Z. R. Wang, J. B. Su, T. Lei and C. B. Wang, Universal strategy to prepare a flexible photothermal absorber based on hierarchical Fe-MOF-74 toward highly efficient solar Interfacial seawater desalination, *ACS Appl. Mater. Interfaces*, 2021, **13**, 45944–45956.

49 J. L. Wang, W. K. Wang, L. Feng, J. Z. Yang, W. Li, J. Shi, T. Lei and C. B. Wang, A salt-free superhydrophilic metal-organic framework photothermal textile for portable and efficient solar evaporator, *Sol. Energy Mater. Sol. Cells*, 2021, **231**, 111329.

50 J. L. Wang, W. K. Wang, X. Y. Mu, Z. T. Li and C. B. Wang, Hexagonal cluster Mn-MOF nanoflowers with super-hydrophilic properties for efficient and continuous solar-driven clean water production, *Sustain.Energy Fuels.*, 2021, **5**, 1995–2002.

51 F. Wang, C. B. Wang, D. Wei, G. F. Li, W. H. Zhang and Z. X. Zhao, Engineering thin water film and cluster evaporation towards extraordinarily high 2D solar vapor generation, *Mater. Today*, 2025, 1369–7021.

52 W. Wang, Z. Y. Tian, X. Huan, Y. H. Li, J. Fan and X. Wang, Solar-driven interfacial evaporation: Material types, structural strategies, and emerging applications, *Langmuir*, 2025, **41**, 24097–24134.

53 L. Zhou, Y. L. Tan, J. Y. Wang, W. C. Xu, Y. Yuan, W. S. Cai, S. N. Zhu and J. Zhu, 3D self-assembly of aluminium nanoparticles for plasmon-enhanced solar desalination, *Nat. Photonics*, 2016, **10**, 393–398.